REPORT DOCUMENTATION PAGE

Form Approved OMB NO. 0704-0188

1. REPORT DATE (DD-MM-YYYY)	2. REPORT TYPE	3. DATES COVERED (From - To)
22-05-2012	Final Report	20-Sep-2010 - 31-Aug-2011

4. TITLE AND SUBTITLE	5a. CONTRACT NUMBER
Low-Loss and Broadband Metamaterials for Negative Index and Transformational Optics Applications	W911NF-10-1-0492
	5b. GRANT NUMBER
	5c. PROGRAM ELEMENT NUMBER
	611102

6. AUTHORS	5d. PROJECT NUMBER
Kevin J. Webb	
	5e. TASK NUMBER
	5f. WORK UNIT NUMBER

7. PERFORMING ORGANIZATION NAMES AND ADDRESSES	8. PERFORMING ORGANIZATION REPORT NUMBER
Indiana University - Purdue University Fort Wayn Sponsored Programs Services Young Hall, 302 Wood Street West Lafayette, IN 47907 -2108	

9. SPONSORING/MONITORING AGENCY NAME(S) AND ADDRESS(ES)	10. SPONSOR/MONITOR'S ACRONYM(S)
U.S. Army Research Office P.O. Box 12211 Research Triangle Park, NC 27709-2211	ARO
	11. SPONSOR/MONITOR'S REPORT NUMBER(S)
	58292-PH-II.6

12. DISTRIBUTION AVAILIBILITY STATEMENT

Approved for Public Release; Distribution Unlimited

13. SUPPLEMENTARY NOTES

The views, opinions and/or findings contained in this report are those of the author(s) and should not contrued as an official Department of the Army position, policy or decision, unless so designated by other documentation.

14. ABSTRACT

Our focus has been on the design and analysis of metamaterials that will lead to the realization of new classes of devices. In large part, the materials are not defined by lithography, and hence are amenable to inexpensive large-scale manufacture. Nonlinear optimization methods have been used to design structures that are based on anisotropic metamaterials and operate as efficient energy collectors (anti-reflection coatings) and cloaks. Active quantum dot metamaterials have yielded controllable

15. SUBJECT TERMS

Optical materials, metamaterials, nanophotonics, energy, forces

16. SECURITY CLASSIFICATION OF:			17. LIMITATION OF ABSTRACT	15. NUMBER OF PAGES	19a. NAME OF RESPONSIBLE PERSON
a. REPORT	b. ABSTRACT	c. THIS PAGE			Kevin Webb
UU	UU	UU	UU		19b. TELEPHONE NUMBER
					765-494-3373

Standard Form 298 (Rev 8/98)
Prescribed by ANSI Std. Z39.18

Report Title

Low-Loss and Broadband Metamaterials for Negative Index and Transformational Optics Applications

ABSTRACT

Our focus has been on the design and analysis of metamaterials that will lead to the realization of new classes of devices. In large part, the materials are not defined by lithography, and hence are amenable to inexpensive large-scale manufacture. Nonlinear optimization methods have been used to design structures that are based on anisotropic metamaterials and operate as efficient energy collectors (anti-reflection coatings) and cloaks. Active quantum dot metamaterials have yielded controllable transmission windows, and this material forms the basis of a nanophotonic source.

A graphene stack is proposed that appears to be the blackest material, and an experimental effort has started with a collaborator. Magnetism based on carbon nanotube coils is providing new insight into magnetic metamaterials. A study of electromagnetic energy in dispersive materials has produced some surprising results. A rigorous study of electromagnetic forces in positive and negative refractive index materials shows that a negative force occurs in a material with gain. Imaging and antenna opportunities are described for metal-insulator stack lenses, and analytic models are developed for curved stacks that can be used in design. The influence of surface roughness on the homogenized anisotropic response of metal-insulator stacks is evaluated.

The people involved in this work were Ph.D. students Shivanand (to complete his Ph.D. in 2012), Sangsik Kim, and Huikan Liu (Ph.D., 2011) postdoctoral scientist Alon Ludwig, and Kevin Webb. Six journal papers were published acknowledging this grant, and others will follow based on the work described in this report.

Enter List of papers submitted or published that acknowledge ARO support from the start of the project to the date of this printing. List the papers, including journal references, in the following categories:

(a) Papers published in peer-reviewed journals (N/A for none)

Received		Paper
2012/05/22 1	5	Kevin J. Webb, Shivanand. Electromagnetic field energy density inhomogeneous negative index materials, Optics Express, (05 2012): 11370. doi:
2012/05/22 1	1	Alon Ludwig, Kevin J. Webb. Dark materials based on graphene sheet stacks, Optics Letters, (01 2011): 0. doi: 10.1364/OL.36.000106
2012/05/22 1	2	Shivanand, Kevin Webb. Negative electromagnetic plane-wave force in gain media, Physical Review E, (11 2011): 0. doi: 10.1103/PhysRevE.84.057602
2012/05/22 1	4	Huikan Liu, Kevin J. Webb. Resonance cones in cylindrically anisotropic metamaterials: a Green's function analysis, Optics Letters, (01 2011): 0. doi: 10.1364/OL.36.000379
2012/05/22 1	3	Huikan Liu, Kevin J. Webb. Resonance cone formation in a curved cylindrically anisotropic metamaterial film, Optics Letters, (01 2011): 0. doi: 10.1364/OL.36.000343

TOTAL: **5**

Number of Papers published in peer-reviewed journals:

(b) Papers published in non-peer-reviewed journals (N/A for none)

Received	Paper

TOTAL:

Number of Papers published in non peer-reviewed journals:

(c) Presentations

Number of Presentations: 0.00

Non Peer-Reviewed Conference Proceeding publications (other than abstracts):

<u>Received</u>   <u>Paper</u>

   TOTAL:

Number of Non Peer-Reviewed Conference Proceeding publications (other than abstracts):

Peer-Reviewed Conference Proceeding publications (other than abstracts):

<u>Received</u>   <u>Paper</u>

   TOTAL:

Number of Peer-Reviewed Conference Proceeding publications (other than abstracts):

(d) Manuscripts

<u>Received</u>   <u>Paper</u>

   TOTAL:

Number of Manuscripts:

Books

<u>Received</u>   <u>Paper</u>

   TOTAL:

Patents Submitted

Patents Awarded

Awards

Graduate Students

NAME	PERCENT_SUPPORTED
FTE Equivalent:	
Total Number:	

Names of Post Doctorates

NAME	PERCENT_SUPPORTED
Alon Ludwig	0.00
FTE Equivalent:	**0.00**
Total Number:	**1**

Names of Faculty Supported

NAME	PERCENT_SUPPORTED
FTE Equivalent:	
Total Number:	

Names of Under Graduate students supported

NAME	PERCENT_SUPPORTED
FTE Equivalent:	
Total Number:	

Student Metrics
This section only applies to graduating undergraduates supported by this agreement in this reporting period

The number of undergraduates funded by this agreement who graduated during this period: 0.00

The number of undergraduates funded by this agreement who graduated during this period with a degree in science, mathematics, engineering, or technology fields: 0.00

The number of undergraduates funded by your agreement who graduated during this period and will continue to pursue a graduate or Ph.D. degree in science, mathematics, engineering, or technology fields: 0.00

Number of graduating undergraduates who achieved a 3.5 GPA to 4.0 (4.0 max scale): 0.00

Number of graduating undergraduates funded by a DoD funded Center of Excellence grant for Education, Research and Engineering: 0.00

The number of undergraduates funded by your agreement who graduated during this period and intend to work for the Department of Defense 0.00

The number of undergraduates funded by your agreement who graduated during this period and will receive scholarships or fellowships for further studies in science, mathematics, engineering or technology fields: 0.00

Names of Personnel receiving masters degrees

NAME
Shivanand
Total Number: **1**

Names of personnel receiving PHDs

NAME
Huikan Liu
Total Number: **1**

Names of other research staff

NAME	PERCENT_SUPPORTED
FTE Equivalent:	
Total Number:	

Sub Contractors (DD882)

Inventions (DD882)

Scientific Progress

See Attachment

Technology Transfer

Low-Loss and Broadband Metamaterials for Negative Index and Transformational Optics Applications

Kevin J. Webb

School of Electrical and Computer Engineering

Purdue University

Email: webb@purdue.edu

May 22, 2012

Summary

Our focus has been on the design and analysis of metamaterials that will lead to the realization of new classes of devices. In large part, the materials are not defined by lithography, and hence are amenable to inexpensive large-scale manufacture. Nonlinear optimization methods have been used to design structures that are based on anisotropic metamaterials and operate as efficient energy collectors (anti-reflection coatings) and cloaks. Active quantum dot metamaterials have yielded controllable transmission windows, and this material forms the basis of a nanophotonic source. A graphene stack is proposed that appears to be the blackest material, and an experimental effort has started with a collaborator. Magnetism based on carbon nanotube coils is providing new insight into magnetic metamaterials. A study of electromagnetic energy in dispersive materials has produced some surprising results. A rigorous study of electromagnetic forces in positive and negative refractive index materials shows that a negative force occurs in a material with gain. Imaging and antenna opportunities are described for metal-insulator stack lenses, and analytic models are developed for curved stacks that can be used in design. The influence of surface roughness on the homogenized anisotropic response of metal-insulator stacks is evaluated.

The people involved in this work were Ph.D. students Shivanand (to complete his Ph.D. in 2012), Sangsik Kim, and Huikan Liu (Ph.D., 2011) postdoctoral scientist Alon Ludwig, and Kevin Webb. Six journal papers were published acknowledging this grant, and others will follow based on the work described in this report.

Contents

1 Optimization of Cloaks and Anti-Reflection Coatings

We have simulated a 2D multilayer cloak wrapped around a perfectly magnetic conducting cylinder with an incident TM plane wave as shown in Fig. 1. Each cylindrical layer of the cloak in Fig. 1(a) has piecewise constant material parameters ϵ_r, ϵ_ϕ and μ_z. The material values were obtained using our optimization procedure and by sampling the continuous material parameters of Pendry's original 2D cylindrical cloak at the middle of each layer. The optimization was achieved using a nonlinear constrained optimization procedure that was coupled with a forward finite element solver, with a cost function $c(\underline{\epsilon}_r, \underline{\epsilon}_\phi, \underline{\mu}_z)$ defined as an azimuthal integration over the radar cross section (RCS) of the cloaked cylinder,

$$c(\underline{\epsilon}_r, \underline{\epsilon}_\phi, \underline{\mu}_z) = \lim_{r \to \infty} \int_0^{2\pi} \frac{2\pi\sqrt{r} \left| \mathbf{E}^s(r, \phi\,; \underline{\epsilon}_r, \underline{\epsilon}_\phi, \underline{\mu}_z) \right|^2}{\left| \mathbf{E}^i \right|^2} d\phi, \tag{1}$$

where $\underline{\epsilon}_r$, $\underline{\epsilon}_\phi$, and $\underline{\mu}_z$ are vectors containing the respective constitutive parameters of each of the cloak layers, r and ϕ denote the radial and azimuthal coordinates respectively, $\mathbf{E}^s(r, \phi; \underline{\epsilon}_r, \underline{\epsilon}_\phi, \underline{\mu}_z)$ is the scattered field of a cloak defined by $(\underline{\epsilon}_r, \underline{\epsilon}_\phi, \underline{\mu}_z)$ at the coordinate (r, ϕ), and $\mathbf{E}^i$ is the incident field. Fig. 1(b) shows the RCS of the cloaked cylinder both before and after optimization for different number of layers in the cloak discretization. It is evident from this figure that the optimization procedure improves the performance of the cloak even when it is discretized into a small number of layers, but as the number of layers is increased, the correspondingly larger number of degrees of freedom in the optimization helps in achieving substantial improvement. Fig. 1(c) gives the simulated magnetic scattered field from a cloaked cylinder comprising 8 layers both before and after optimization. This figure clearly shows that the optimized cloak induces reduced scattering even in the near field.

Using the complex constraint for the minimization, another cloak optimization has been studied. These constraints are related with physical fabrication limits and lead to cloak designs that can be realized using current fabrication tools and materials. An example for such a constraint is the dynamic range of the anisotropic material properties that could be obtained using layered metal-insulator stacks, a structure we have been studying recently [1]. An initial estimate for this dynamic range has been obtained, assuming effective medium conditions and a large cloak radius of curvature, from the dielectric constants of a 1-D metal-insulator stack. The frequency-dependent anisotropic dielectric constants for an alternating stack of silver and magnesium oxide (MgO) for different metal duty cycles D are shown in Fig. 2(a). From Fig. 2(a), the dispersion will be smallest (and thus, the cloaking performance will be relatively wideband) if operation is beyond resonance, i.e., in the longer wavelength range. This regime gives a dielectric constant parallel to the stack interface ($\epsilon_\parallel$) which is smaller than that perpendicular to the interface ($\epsilon_\perp$). Keeping the cloak non-magnetic, good performance can be achieved with Ag and MgO layers stacked azimuthally (see Fig. 2(b)), thereby achieving a radial dielectric constant that is smaller than the azimuthal dielectric constant. The next step toward realizing an optical cloaking device will be to use the bounds on the dynamic range of the anisotropic material properties of the cloak envisioned in Fig. 2(b) as constraints for the optimization procedure aimed at the design of an efficient cloak. To exemplify the cloak performance using the suggested optimization procedure, even when the initial material parameters stem from the reduced nonmagnetic cloak parameter set and the optimization is constrained to keep the cloak nonmagnetic, Fig. 2(c) shows the RCS of the nonmagnetic cloaked cylinder both before and after optimization for 8 layers in the cloak discretization. The dramatic improvement in the cloaking performance when optimizing a cloak based on the nonmagnetic reduced material properties [2] encourages us to believe

that the implementation of the bounds of the dynamic range of metal-insulator stacks as constraints for the optimization procedure will yield effective and realistic cloaking.
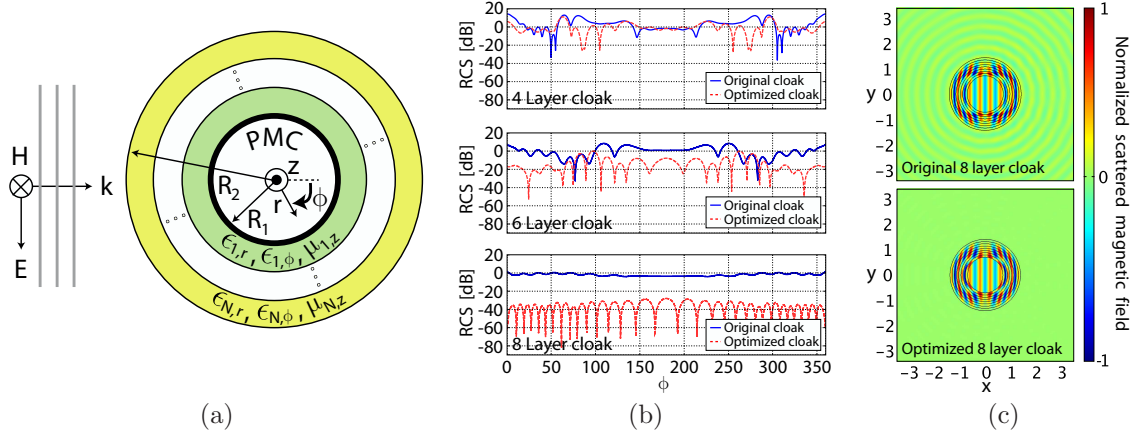

Figure 1: (a) A two-dimensional N layer cloak wrapped around a perfectly magnetic conducting cylinder with an incident TM plane wave impinging from the left. (b) Simulated RCS of a cloaked cylinder with inner radius of $R_1 = 700$ nm and outer radius of $R_2 = 1400$ nm, illuminated at $\lambda = 400$ nm. The cloak is discretized into 4, 6 and 8 layers, each shown in a different panel in which the continuous blue line corresponds to the result by discretizing Pendry's original 2D cloak [3] and the doted red line corresponds to cloak parameters obtained using optimization. (c) Simulated scattered magnetic field for the 8 layer cloak with the same geometry and incidence as in (b), before (top) and after (bottom) the optimization process. The total field inside the cloaked region is zero because the scattered field (shown) cancels the incident field.
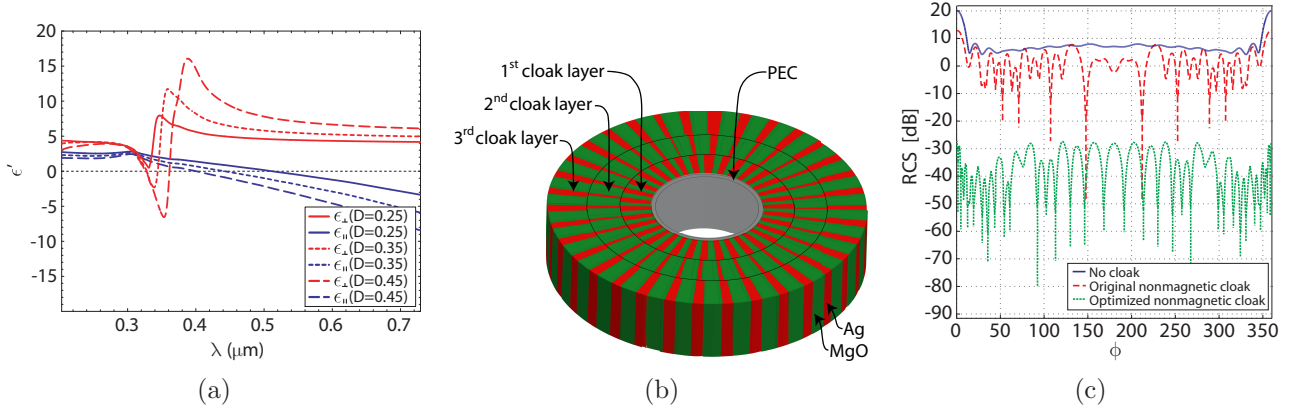

Figure 2: (a) Calculated real dielectric constants $\epsilon_\parallel$ and $\epsilon_\perp$, parallel and perpendicular to the surface of the effective slab, for a Ag/MgO stack with Ag volume fraction D, using published data. (b) Conceptual illustration of a cloak built out of silver and magnesium oxide stacks. (c) Simulated RCS (dB) of a 700 nm thick nonmagnetic cloak wrapped around a PMC cylinder of 1400 nm in diameter that is illuminated at $\lambda = 400$ nm. The cloak is discretized into 8 layers. The continuous blue curve corresponds to the RCS of only the PMC cylinder without a cloak, the dashed red curve corresponds to the RCS of a PMC cylinder covered by a cloak with parameters obtained by discretizing the reduced nonmagnetic 2D cloak suggested in [2] and the doted green curve corresponds to a PMC cylinder covered by a nonmagnetic cloak with optimized parameters.
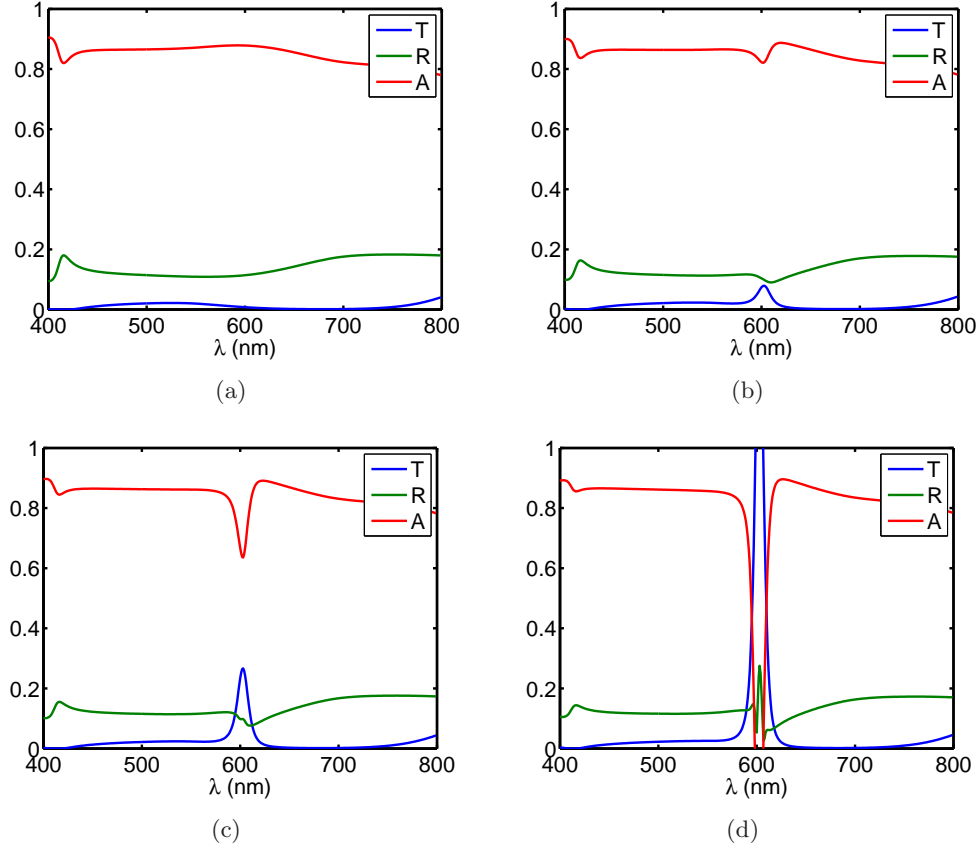
2

Figure 3: Power transmission (T), reflectance (R), and absorption (A) for a 2 μm thick planar slab composed of QD/Ta mixture as a function of the incident wavelength λ for varying excited QD fraction. The percentage of excited QDs were chosen to be (a) 0% (b) 25% (c) 37.5% and (d) 55%. The fill fraction of tantalum (Ta) and CdSe QDs in an SiO_2 background is 0.16 and 0.04, respectively. Note the opening of the transmission window in the slab with the increase in the percentage of the excited QDs in the mixture.

2   Active Quantum Dot Optical Metamaterials

Realizing an active metamaterial composed of a semiconductor quantum dot (QD) and metal nanoparticle mixture provides important frequency-selective gain and loss properties, depending on size and composition, and with optical (or ultimately electrical) pumping, the metamaterial response can be controlled. For example, it is in principle possible to achieve a lossless metal, and this would revolutionize plasmonics and open new domains for ultrafast signal processing and sensing. The material is also key to nanophotonic sources and detectors, because of compatibility of fabrication with plasmonic materials. Particularly useful is the control over the loss and gain with the narrow exciton level in the QD, making possible dispersion engineering and a lossless local metallic response. We are pursuing an experimental effort to demonstrate QD metamaterials with important characteristics in applications.

Our preliminary studies show that using the properties of an active QD mixture, it is possible to achieve a material response with a narrowband transmission window while maintaining low reflectance. Figure 3 shows the calculated power transmission (T), reflectance (R), and absorption (A) of an example QD/metal mixture slab, placed in vacuum, for different fractions of excited QDs in the mixture. This result uses tantalum (Ta) as the metal, offering high broadband absorption, and
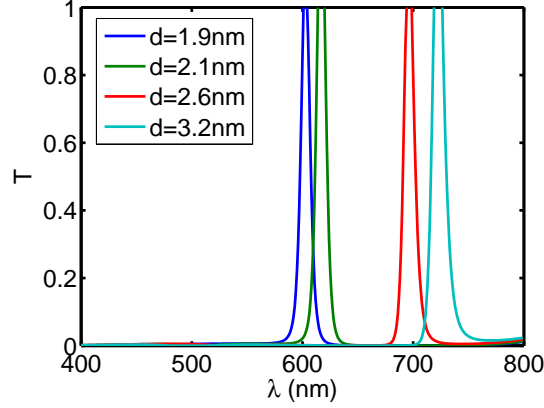
3

Figure 4: Shift in the central wavelength of the power transmission window with the change in the diameter, d, of the QDs used in the gain mixture in the 2 μm thick planar slab. The fill fraction of tantalum (Ta) and CdSe QDs in SiO_2 background was 0.16 and 0.04, respectively. The percentage of excited QDs was chosen to be 55% for each case.

CdSe QDs as the gain material to open up the transmission window. The fill fraction of Ta and CdSe QDs in an SiO_2 background for all the cases presented is 0.16 and 0.04, respectively. The QDs have a diameter of 1.9 nm and the dielectric constant was obtained using our simplified QD permittivity model [4]. The effective permittivity for the mixture was then obtained using the Maxwell Garnett mixing formula with three species (tantalum, gain QDs and loss QDs) in the SiO_2 background [4]. The power transmission and reflection for the planar isotropic slab is calculated using the standard transmission and reflection formulas with a normally incident plane wave [5]. From Fig. 3, a transmission window opens as the pump energy is increased or with an increase in the fraction of the excited QDs in the mixture. In this example of a 2 μm thick slab, the QDs provide the gain window and the Ta nanoparticles, which constitute 16.0 % of the mixture, absorb most of the energy at other frequencies. The overall effect of the mixture allows us to open a narrow transmission window by tuning the excited QD concentration using different pump energies. Figure 4 shows the shift in the central wavelength of the transmission window with the change in the diameter, d, of the QDs used in the gain mixture of the 2 μm thick planar slab. The fill fraction of tantalum and CdSe QDs in the SiO_2 background was again 0.16 and 0.04, respectively, and 55% of QDs were assumed to be excited. The center of the transmission window shifts to longer wavelength with an increase in the diameter of the QDs. A proper choice of the QD diameter and the metal nanoparticle can theoretically allow us to open up a transmission window at any specific wavelength.

Another application for active QD metamaterials is as the gain medium in a plasmonic amplifier. Surface plasmon waves at metal surfaces allow light to be tightly confined, and various waveguide configurations provide great potential for future optical devices. With active optical metamaterials having low loss or even overall gain, the propagation length of the surface plasmon waves can be significantly enhanced. Also, with an active metamaterial having overall gain inside a plasmonic cavity, a nano-laser can be achieved. We have studied the use of a quantum dot (QD) and dielectric mixtures in a metal slot cavity to create a plasmonic amplifier. We have previously reported that a small resonant cavity, with the gap size much smaller than wavelength, is capable of confining the light and providing highly localized resonant field enhancement for specific nanoparticle structures [6, 7]. The cavity resonant length can be predicted using the wavelength of the dominant propagating waveguide mode. The cavity quality factor (Q) is dictated by the geometry and the complex dielectric constant of the metal. In designing and simulating active plasmonic devices, the material properties,
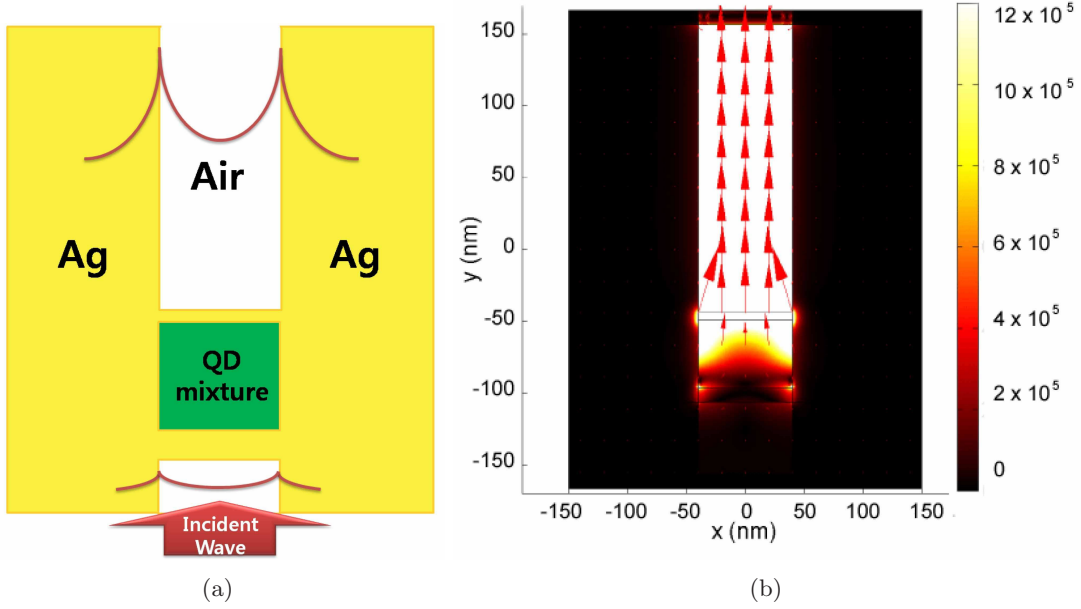
4

Figure 5: (a) Schematic view of a MIM waveguide cavity amplifier with a CdSe/SiO$_2$ QD mixture. (b) FEM simulation of the total power flow magnitude [W/m^2] for red light (λ= 633 nm). The absorption coefficient for these QDs in a SiO$_2$ background was found to be 1.1×10^7 m^{-1} at the pump wavelength of 532 nm [8] with a QD fill fraction of 0.3. Using this and a pump volume of 1.57×10^{-17} m^3 requires 0.17 W to pump 60% of the QDs.

especially of the gain medium, are very important. Our previous work on modeling the dielectric constant of QD mixtures [4] played a key role in this work. We used Maxwell Garnett mixing with a model for the QD dielectric constant, along with experimental QD data for commercially available QDs. The QD amplifier we consider uses a (metal-insulator-metal) MIM waveguide, and a schematic of the structure is shown in Fig. 5(a). The cavity Q has been enhanced by placing two partially reflecting metal mirrors at each end of the cavity, as shown in Fig. 5(a). An finite element method (FEM) simulation was carried out to study the amplification from such an active cavity, and the magnitude of the total power flow for the amplifier is shown in Fig. 5(b). The fill fraction of QDs (having diameter 2.1 nm) in the SiO$_2$ background is 0.3, and the homogenized effective permittivity of the mixture is from Maxwell Garnett mixing with two species (gain and loss QDs). A series of such FEM simulations with varying wavelength λ illustrates the amplification inside the cavity as a function of the incident signal wavelength, and the results are shown in Fig. 6. The fraction of excited QDs in the mixture is dependent on the pump energy, which can be tuned to obtain different homogenized dielectric constants for the QD mixture. From Fig. 6, it is clear that as we increase the excited QD concentration, the amplification of the signal in the cavity increases.

These examples illustrate the potential of QD metamaterials. We have proposed an idealized model for the dielectric constants of active QDs (see [4]), and now we are pursuing experiments to better characterize the QDs by matching our model parameters to the experimental data. This will place us in a position to be able to accurately design material responses for several key demonstrations that will open new application domains.
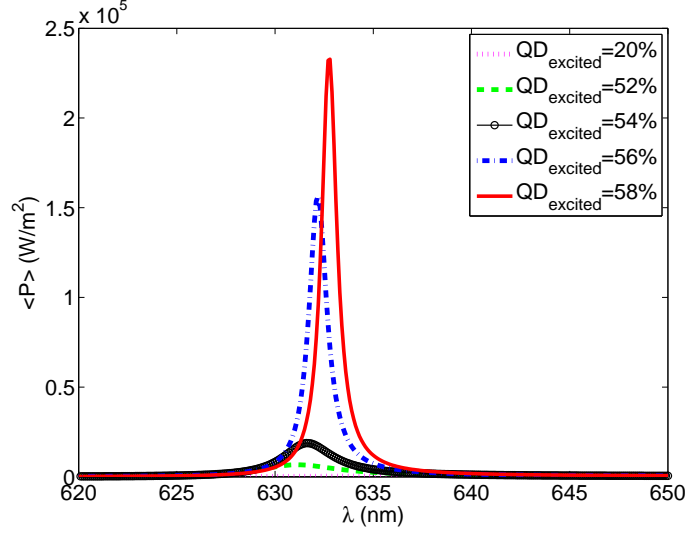
5

Figure 6: Total magnitude of the emitted power from an amplifier cavity (shown in Fig. 5(a)) as a function of the incident wavelength λ for different fractions of excited QDs in the mixture. The simulation parameters remained the same as for Fig. 5(a)), except that the percentage of excited QDs in the mixture is varied. The fraction of the excited QDs can be tuned by tuning the pumping energy.

3 Black Materials Based on Graphene Stacks

Relying on recent developments in theory and measurement of the properties of graphene sheets [9–11], we have been able to calculate the effective medium parameters for a one dimensional stack of graphene sheets separated by an arbitrary substance (see Fig 7(a)) [12]. As the surface conductivity of a single graphene sheet is very close to the universal value of $\sigma_0 = \pi e^2/2h$ throughout a substantial portion of the optical regime (250 nm-6000 nm), the effective parameters of the stack vary linearly and rather slowly with frequency for visible light. A few conditions must hold in order for the electromagnetic homogenization to be valid [13]. First, the distance between the graphene sheets must be large enough compared to the interatomic distance ($\sim$ 0.3 nm) to avoid mutual effects causing a change in the electronic structure of the sheets. Two other conditions stem from the need for a meaningful homogenization of the stack bounding both the distance between the sheets and the conductance of each sheet to be small. We show that for visible and near-infrared light incident on a stack immersed in a low refractive index medium, all those conditions hold when the distance between the sheets is in the range 1 nm $< d < \lambda_0/10$ nm. A low refractive index medium is crucial for the performance of such a graphene stack as a dark material, and we assume that due to the remarkable mechanical strength of the sheets, it is possible to use a sparsely populated matrix of small and low refractive dielectric elements in air as separating layers between graphene sheets. Such separating layers will have effective medium parameters close to those of free space. Recent developments in graphene shape control [14] indicate that the manufacturing and handling of graphene has reached the stage where the creation of the above stacks is possible. For simplicity we treat the layers between the graphene sheets as free space when calculating the effective medium parameters. Assuming also sheet conductivity of σ_0 and inter-sheet distances d that are within the
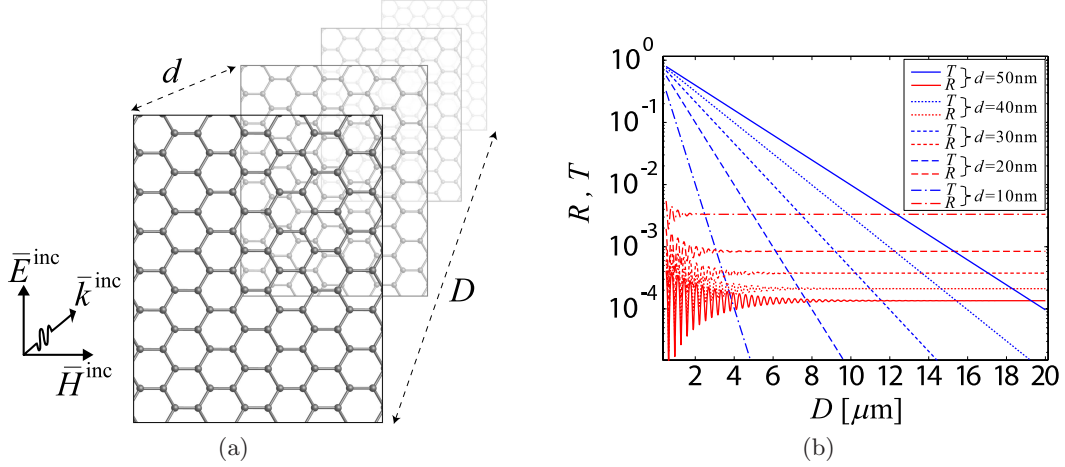
6

Figure 7: (a) Sketch of the graphene stack structure. (b) Normalized reflected and transmitted power for a graphene stack illuminated by a plane wave in a frequency corresponding to red light ($\lambda = 630$ nm) as a function of the stack thickness D for different inter-sheet distances d.

above range of meaningful homogenization, we find that

$$\epsilon_t = 1 + \frac{2i}{\gamma}, \quad \text{where} \quad \gamma = \frac{2k_0 d}{\pi\alpha} \quad \text{and} \quad \alpha = \frac{\sigma_0}{\pi\epsilon_0 c}. \tag{2}$$

Here, ϵ_t is the transversal component of the anisotropic relative effective permittivity and α is the fine structure constant. The other relative effective parameters of the stack are the normal component of the permittivity $\epsilon_n = 1$ and the permeability $\mu = 1$. The anisotropic imaginary part of the transversal permittivity can be easily understood as stemming from the conductivity of the sheets in the transverse direction. Electric fields normal to the sheets will not induce currents and thus only the transverse component of the permittivity is affected by the existence of the sheets.

Figure 7(b) shows the normalized reflected and transmitted power for a graphene stack illuminated by a plane wave in a frequency corresponding to red light ($\lambda = 630$ nm) as a function of the stack thickness (D) for stacks of different inter-sheet distances (d). It is evident that as the thickness of the stack (D) increases, the dominant portion of power that is not absorbed in the stack is due to reflection at the interface of the stack. Next, we compare those results to the theoretical results given in [15] for p-polarized incident plane-waves impinging a medium comprising an array of aligned nanotubes of 10 nm diameter and having a 50 nm array spacing. In order to achieve the same low reflectivity (0.02%) obtained for the nanotube array using the stack, we need to place the sheets at a distance of $d = 41.2$ nm. This yields an absorption coefficient 5 times larger than that of the nanotube array. Such a large absorption coefficient implies that we could use a much thinner coating in order to achieve properties similar to those of the nanotube array. By increasing the inter-sheet distance (d), the reflectivity is reduced, however, this has the detrimental effect of a decrease in the absorption coefficient. Thus, by increasing the inter-sheet distance (d), together with the entire thickness of the stack, one can increase the blackness of the resulting stack without bound. Note that when d is no longer small compared to the wavelength, the homogenization and effective properties we obtained are no longer valid. However, we suspect that the physical mechanism making the material black will still make the materials darker, and we plan to study the interpretation when not in the homogenization regime. Another way to increase the material blackness would be to reduce the reflectivity at the first few layers and absorb the light in the bulk of the stack. To this end, we suggest to continuously reduce the inter-sheet distance (d) with spatial location, and to optimize the functional change in d to improve the blackness.

We are working with Professor Zhihong Chen at Purdue and one of her students on a fabrication

method for the graphene stack. Beyond black materials, this demonstration will provide a high-speed photodetector material and may also prove valuable in electrodes for solar cells.

4 Optical and Terahertz Magnetic Materials

We suggest a cellular structure where each cell comprises a single carbon nanotube (CNT) coil, and each pair of neighboring cells are of different handedness (i.e., left-hand and right-hand coils, as in Fig. 8(a)). This structure is on average symmetric with respect to mirror reflection, and thus non-chiral. We have studied the homogenized permeability of a supercell of 8 CNW coils, shown in Fig. 8(b), in a doubly periodic lattice. We used a vector electromagnetic solution and a parameter extraction procedure similar to the one used in [16], as a function of material thickness, in order to establish converged bulk parameters. To simplify our initial calculations and obtain results that are dependent only on the ratio between dimensions and wave-length, we used classical graphite properties for the coils and assumed a small skin depth compared with coil wire thickness. This simplification allowed us to concentrate on the choice of coil and cell dimensions that will decrease the resonant frequency while keeping the coil to coil interaction weak, so that the effective medium parameters will converge even for small material thickness. The result in Fig. 8(c) shows the real and imaginary components of the homogenized permeability as having a resonance, and that it is a metamaterial. It would therefore appear that a mixture of CNT coils could provide negative μ at THz frequencies with an appropriate geometry. We also found that the resonant frequency in the homogenized result is insensitive to source polarization and orientation, which is very important for random mixtures. Our results on magnetism from CNT coils are being developed for a journal paper.
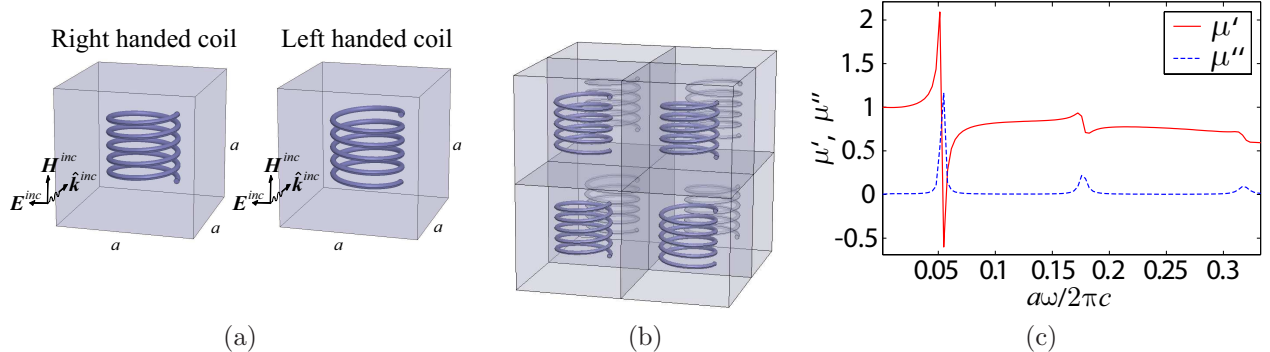

Figure 8: (a) Left-handed and right-handed carbon coils that are placed in $a \times a \times a$ cells. The coil diameter and length is $0.5a$, and the wire diameter is $0.02a$. (b) Non-chiral unit-cell of periodic metamaterial that comprises 4 left-handed coils and 4 right-handed coils. (c) Real (μ') and imaginary (μ'') components of the effective permeability of the coil metamaterial, obtained using a scattering model.

5 Electromagnetic Energy in Dispersive Materials

A negative refractive index can be achieved when both the dielectric constant ϵ and the permeability μ are negative, which requires an operating frequency near a resonance in both constitutive parameters. In this frequency regime, the material properties can be highly dispersive for the candidate metamaterials, and the loss can be substantial. Loudon [17], Ruppin [18], Tretyakov [19], Boardman and Marinov [20], Cui and Kong [21], and Nunes *et al.* [22] and several others have studied energy density issues in dispersive media. This substantial body of work presents results where all energies

(total, stored and dissipated) remain positive. However, Ziolkowski [23] questions whether the electromagnetic energy must remain positive. We have shown that the electric field energy density in dispersive materials can be exactly separated into stored and lost energies when using the electric field as the basis [24]. Our analytical and numerical results for a narrowband modulated wave near a material resonance indicated that the stored energy can be negative, while the total energy remains positive in this high-loss regime. We have obtained the energy density for a negative refractive index material. For the special case of a frequency-independent wave impedance in the material, the exact separation of both electric and magnetic energy densities into stored (electric and magnetic) and lost (electric and magnetic) densities is shown to be possible.

Using Poynting's theorem, the time derivative of electric, u_E, and magnetic, u_H, field energy densities can be expressed as

$$\frac{\partial u_E}{\partial t} \equiv \mathbf{E} \cdot \frac{\partial \mathbf{D}}{\partial t} \ \text{ and } \ \frac{\partial u_H}{\partial t} \equiv \mathbf{H} \cdot \frac{\partial \mathbf{B}}{\partial t}. \tag{3}$$

Expressing the electric flux density as an exact Fourier superposition using the complex material constitutive parameters and choosing the electric field as the basis (see [24] for details), we have shown that the electric field energy density can be separated into the stored and lost electric field energy densities. Similarly for the magnetic field case, with magnetic the field as the basis, the magnetic field energy density has been separated into the stored and lost magnetic field energy densities [25].

The electric and magnetic fields are related through $H(t) = (1/2\pi) \int_{-\infty}^{\infty} E(\omega) \eta^{-1}(\omega) e^{-i\omega t} d\omega$, where $\eta(\omega)$ is the frequency-dependent wave impedance. When the electric field is chosen as the basis, u_E is exactly separable into w_E (stored electric field energy) and q_E (lost electric field energy), but u_H is generally not. Similarly, when the magnetic field is chosen as the basis, u_H is exactly separable. However, in the special case when both $\epsilon(\omega)$ and $\mu(\omega)$ are constant or $\epsilon(\omega) = \mu(\omega)$, $\eta(\omega)$ is independent of frequency, giving $H(t) = \eta E(t)$, where η is the constant value of the wave impedance in the frequency domain. For this case, the total energy density, $u = u_E + u_H$, is exactly separable into stored (which is returned to the field, $w = w_E + w_H$) and lost (converted to a non-electromagnetic form, $q = q_E + q_H$) energies.

We assume $E = e(t)\cos(\omega_0 t)$, with slowly varying modulation signal $e(t)$ relative to $t_0 = 2\pi/\omega_0$, producing an effective bandwidth that is small relative to the features of $\epsilon(\omega)$. Following our earlier work [24], the approximate form of $\partial D/\partial t$ is obtained by using the first two terms in the Taylor series expansion of $(\omega + \omega_0)\epsilon(\omega + \omega_0)$ about $\omega = 0$. The product of $E(t)$ and the approximate form of $\partial D/\partial t$ gives the approximate form of $\partial u_E/\partial t$. After some additional steps (see [24]), we obtain the average electric field energies

$$\langle w_E \rangle \approx \frac{1}{4}\epsilon_0 \left. \frac{\partial \left[\omega \epsilon'(\omega) \right]}{\partial \omega} \right|_{\omega_0} e^2(t) \tag{4}$$

$$\langle \frac{\partial q_E}{\partial t} \rangle \approx \frac{1}{2}\omega_0 \epsilon_0 \epsilon'' e^2(t). \tag{5}$$

Following a similar analysis using the magnetic field as the basis instead of the electric field, we obtain the average magnetic field energies

$$\langle w_H \rangle \approx \frac{1}{4}\mu_0 \left. \frac{\partial \left[\omega \mu'(\omega) \right]}{\partial \omega} \right|_{\omega_0} h^2(t) \tag{6}$$

$$\langle \frac{\partial q_H}{\partial t} \rangle \approx \frac{1}{2}\omega_0 \mu_0 \mu'' h^2(t), \tag{7}$$

9

where $h(t)$ is the slowly varying envelope of the magnetic field. Equations (4) - (7) apply regardless of the degree of loss, provided that the two-term Taylor series expansion for $\partial D(t)/\partial t$ and $\partial B(t)/\partial t$ are sufficiently accurate.

For the simple case when η is independent of frequency and the energy density is exactly separable, we choose identical electric and magnetic susceptibilities ($\chi_E = \chi_M$) in arriving at a negative index material given by $\chi_E(\omega) = a_1 \left(\omega_1^2 - \omega^2 - i\gamma_1\omega\right)^{-1}$. Example dispersive dielectric constant and relative permeability responses are shown in Fig. 9(a). The material parameters are chosen so that $n'(\omega_0) = -1$ for $\omega_0 = 8/7$, where $n'(\omega_0)$ is the real part of the refractive index of the material.

We assume a Gaussian modulated field given by $E(t) = (\sigma\sqrt{2\pi})^{-1} \exp\left[-(t - t_c)^2 (2\sigma^2)^{-1}\right] \cos[\omega_0(t - t_c)]$ with $\omega_0 = 4/9$, $8/7$ and $4/3$, $t_c = 2^{10}(2\pi)$, $\sigma = 2^7(2\pi)$, and carrier phase delay $\omega_0 t_c$. The magnetic field was obtained from the Fourier decomposition of this electric field using $H(\omega) = E(\omega)/\eta(\omega)$. The expression for $\partial u_E/\partial t$ in (3) was evaluated numerically, with $D(t)$ formed by Fourier transforming (using an FFT) the temporal electric field, multiplying by $\epsilon(\omega)$, and then inverse Fourier transforming the result. The quantities $\partial w_E/\partial t$ and $\partial q_E/\partial t$ were formed using the exact decompositions. Numerical integration over time followed by time-averaging over the period t_0 resulted in $\langle w_E \rangle$, $\langle \partial q_E/\partial t \rangle$ and $\langle u_E \rangle$. Using the magnetic field instead of the electric field and following a similar procedure, the average quantities $\langle w_H \rangle$, $\langle \partial q_H/\partial t \rangle$ and $\langle u_H \rangle$ were obtained.

Figure 9(b) shows that when the carrier frequency is sufficiently far from the resonant frequency, $\langle w_E \rangle$ as well as $\langle w_H \rangle$ are positive, just as they would have been in free space. However, when the carrier frequency is just above the resonant frequency ($\omega_0 = 8/7$), and in this case where the refractive index is negative, $\langle w_E \rangle$ as well as $\langle w_H \rangle$ become negative. Figure 9(c) shows the numerical results for $\langle \partial q_E/\partial t \rangle$ and $\langle \partial q_H/\partial t \rangle$ obtained for the same three carrier frequencies, along with the results from the approximate analytical expressions in (5) and (7). Throughout, the total average energy ($\langle u_E \rangle + \langle u_H \rangle$) remains positive, as Fig. 9(d) shows. At times long after the pulse has gone, $\langle q_E \rangle = \langle u_E \rangle$ and $\langle q_H \rangle = \langle u_H \rangle$, indicating that no additional energy beyond that delivered by the electromagnetic field is involved, despite $\langle w_E \rangle$ and $\langle w_H \rangle$ being negative for some time. Notice the excellent agreement between the exact results and the approximate analytical expressions in Figs. 9(b) and 9(c).

The energies represent running totals as a function of time, and the sign of $\partial w/\partial t$ gives the transfer direction of the transient energy, which integrated over time and averaged over the carrier period to give the net energy exchange up to each instant in time. When $\langle \partial w/\partial t \rangle$ is positive during the first half of the Gaussian and negative during the second half, $\langle w \rangle$ in Fig. 9(b) is positive throughout and zero for large time, after the pulse has left that point in space. In the case where we find negative stored energy, near a resonance, $\langle \partial w/\partial t \rangle$ is first negative, and then positive. The negative field energy is energy borrowed from the material, and during the second half of the pulse, the field repays this energy.

6 Electromagnetic Plane Wave Forces in Homogeneous Materials

We consider the various contributions to the electromagnetic force from a fundamental perspective, including the material constitutive parameters and their dispersive properties, and show that the radiation pressure is positive for propagating waves in homogeneous passive media, even when the refractive index is negative [26, 27]. We show, however, that the force can be negative when the medium has gain, and we describe an experiment. Our work provides a foundation for the treatment of forces in dispersive inhomogeneous material systems, such as objects in some background material, and the further study of the influence of the background material properties.
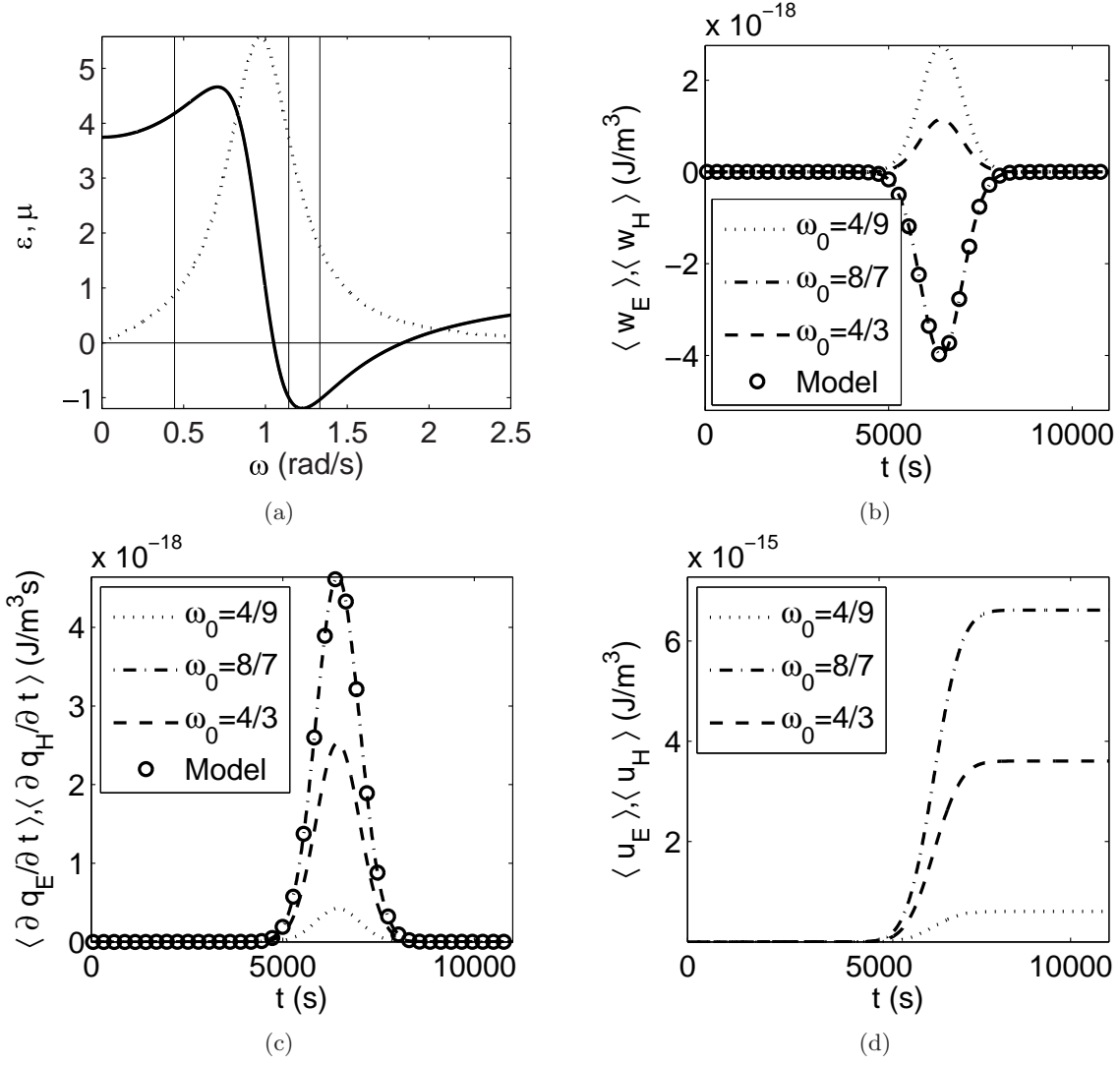
10

Figure 9: (a) Real (solid line) and imaginary (dotted line) part of the dielectric constant and relative permeability $\{\epsilon, \mu\} = 1 + 2.7\omega_1^2(\omega_1^2 - \omega^2 - i0.5\omega)^{-1}$ for $\omega_1 = 1$. The three different carrier frequencies used ($\omega_0 = 4/9, 8/7, 4/3$) are marked by thin vertical solid lines. (b) $\langle u_E \rangle|_{\epsilon''=0} = \langle w_E \rangle$ and $\langle u_H \rangle|_{\mu''=0} = \langle w_H \rangle$ obtained for $\{\epsilon', \mu'\} = \text{Real}\{\epsilon, \mu\}$. The lines give exact numerical results and the model result (circles) plots (4) for the $\omega_0 = 8/7$ case. (c) $\langle \partial u_E/\partial t \rangle|_{\epsilon'=0} = \langle \partial q_E/\partial t \rangle$ and $\langle \partial u_H/\partial t \rangle|_{\mu'=0} = \langle \partial q_H/\partial t \rangle$ obtained with $\{\epsilon'', \mu''\} = \text{Imag}\{\epsilon, \mu\}$. The lines give exact numerical results and the model result (circles) is from (5) for the $\omega_0 = 8/7$ case. (d) Exact time-averaged energy densities, $\langle u_E \rangle$ and $\langle u_H \rangle$, obtained for $\{\epsilon, \mu\}$.

11

The electromagnetic plane wave force density in source-free homogeneous medium is [26]

$$\mathbf{f} = \frac{\partial \mathbf{P}}{\partial t} \times \mu_0 \mathbf{H} - \frac{\partial \mu_0 \mathbf{M}}{\partial t} \times \epsilon_0 \mathbf{E}. \tag{8}$$

For a modulated electric field $\mathbf{E}(t) = \hat{e}\, E(t) = \hat{e}\, e(t) \cos(\omega_0 t)$, we have shown the normalized average force density to be

$$\langle f_n \rangle = (C_1 + D_1)\, e^2(t) + (C_2 + D_2)\, e(t) \frac{\partial e(t)}{\partial t} + C_3 \left[\frac{\partial e(t)}{\partial t}\right]^2, \tag{9}$$

where the constants C's and D's depend on the constitutive material parameters and are defined in Ref. [26].

To evaluate the significance of the force in a homogeneous medium with loss and gain medium, consider a Gaussian modulation signal given by $e(t) = \exp[-t^2 \left(2\sigma^2\right)^{-1}]$, where we use $\sigma = 2^8 \pi$, $\omega_0 = 1$, and $N = 2^{20}$ sample points over a temporal support of $2^{13}\pi$. A numerical simulation was carried out by first evaluating the electric field, then determining the magnetic field using a discrete Fourier transform and by incorporating the frequency-dependent material parameters. Subsequently, the total instantaneous plane wave force was obtained using the scalar form of (8), and this was numerically integrated over time to form $\langle f \rangle$. We describe this evaluation as exact because the accuracy is subject only to numerical precision. The time-average force was also calculated using the analytical model given in (9). To evaluate the coefficients C_2, C_3, and D_2, we used numerical derivatives of $\mu(\omega)$ and $\epsilon(\omega)$. Figures 10(a) and (b) show the time-averaged normalized electromagnetic plane wave force density calculated using the exact numerical procedure (solid line) and the analytical expression in (9) (circles) for a non-magnetic material with $\mu = 1$ and having overall (a) loss, with permittivity ϵ_{loss}, and (b) gain, with permittivity ϵ_{gain}. We set $\epsilon_{loss} \equiv \epsilon = 1 + 2(0.95^2 - \omega^2 - i0.2\omega)^{-1}$ for a passive and lossy two-level system and $\epsilon_{gain} \equiv \epsilon = 1 - 0.6(1.05^2 - \omega^2 - i0.2\omega)^{-1}$ for an active system having overall gain. From Fig. 10, $\langle f_n \rangle$ is positive for the lossy material and negative for the material with gain, throughout the pulse. Notice that the analytical result of (9) is in excellent agreement with the numerical data.

In a physical demonstration of a negative force, the gain medium would be excited to create a population inversion, and this system would be illuminated with a probe electromagnetic wave [26, 27].. The force will be in a direction opposite to the Poynting vector for this probe wave. To evaluate the significance of the negative plane wave force in media with gain, we compared the expected positive force for a metal, which has been measured [28], with the estimated negative force in an excited quantum dot medium [4]. A negative force on a material exhibiting gain can be considered a collective result of the stimulated emission from each atom, where the atomic recoil is in the direction opposite to that of the emitted photons [29].

7 Anisotropic Metamaterials Based on Metal-Insulator Stacks

Multi-layer metal-insulator stacks at infra-red and visible frequencies can be characterized as uniaxially anisotropic metamaterials, provided the periodicity is much smaller than the operating wavelength. Effective medium parameters characterizing the anisotropic media typically involve two variables: $\epsilon_\perp$, the permittivity component perpendicular to the material surface, and $\epsilon_\parallel$, the component parallel to the surface. It has been shown that the strong anisotropy can lead to a wide variety of physical phenomena and important applications. Here we describe two relevant results: subwavelength imaging and a miniaturized spectrometer.
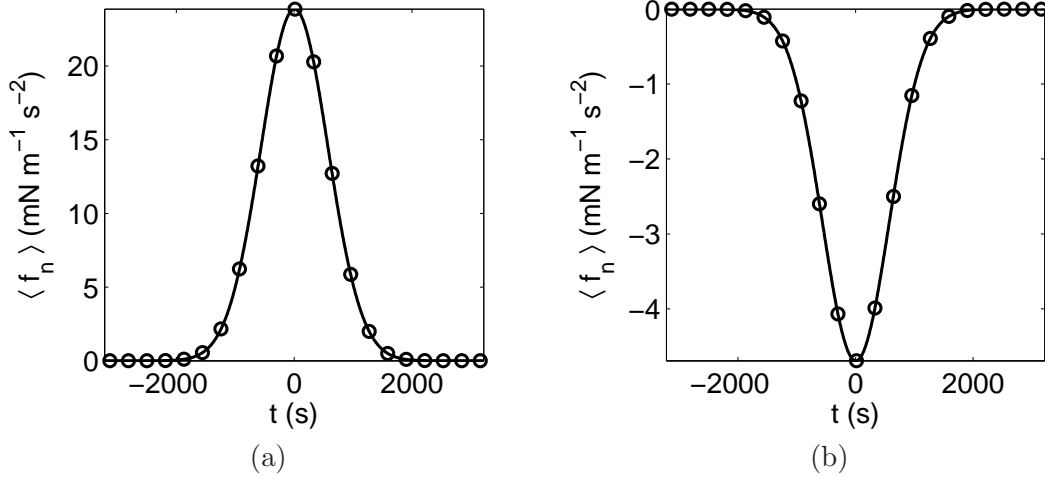
Figure 10: The time-averaged normalized electromagnetic plane wave force density calculated using the exact numerical procedure, shown by solid lines, and the analytical expression in (9), shown by circles, for a non-magnetic material with $\mu = 1$ and having overall (a) loss, with permittivity ϵ_{loss} and (b) gain, with permittivity ϵ_{gain}. The electric field modulation is given by $e_g(t)$, and the carrier frequency is $\omega_0 = 1$.

We have numerically shown a bilayer lens with subwavelength resolution which consists of one anisotropic layer and one isotropic dielectric layer, with leaky waveguide operation of the anisotropic film [30]. In Fig. 11(a), we show the homogenized Ag/SiO_2 metal-insulator stack on a silicon (Si) film as an example. The finite element simulation result clearly demonstrates that the slab behaves as an optical leaky waveguide radiating backwards. Because the leaky mode supported by the system can have $|\operatorname{Re}(k_z)| > k_0$, a planar near-field imaging system that transfers sub-diffraction features can be envisioned by pairing a backward leaky waveguide with a silicon slab, as shown in Figs. 11(b) and 11(c). As illustrated in Fig. 11(b), the waves radiated from the source emerge as strongly confined beams inside the anisotropic slab, and then re-radiate into the backward quadrant at the interface between the anisotropic waveguide and the silicon slab to form a focal point at a certain distance from the interface. In contrast to the realization of a super-resolving lens using stack-based anisotropic bilayer lenses that we have analyzed and developed previously [31], the present approach to subwavelength imaging does not impose any restrictions on impedance match or operating wavelength, and it requires the synthesis of only one anisotropic bulk medium.

We have designed a new spectrometer class that could be realized with TM illumination of a small aperture placed in front of a metal-insulator stack, and we have derived analytical formulations to evaluate the working wavelength range and the wavelength sensitivity [32]. This spatial filtering property is based on the frequency-dependent preferred propagation direction associated with an anisotropic slab, determined by $-\epsilon_x/\epsilon_z$, due to intrinsic material dispersion. As an example, we investigated a Ag/ZnO metal-insulator stack as a possible realization of $\epsilon_x\epsilon_z < 0$ for the spectrometer. Figure 12(a) depicts the frequency response of the homogenized Ag/ZnO stack at the output plane for three different wavelengths, and compares the magnitude of the transmitted electric fields employing the closed-form solution we developed (for design purposes), which we derived based on a Green's function analysis [32], and full-wave finite element simulation results. In Fig. 12(b), we plot the position of the major peak as a function of wavelength, showing that the principal peak continuously shifts away from the center as wavelength increases, and that a larger slab thickness gives rise to larger peak shifts.
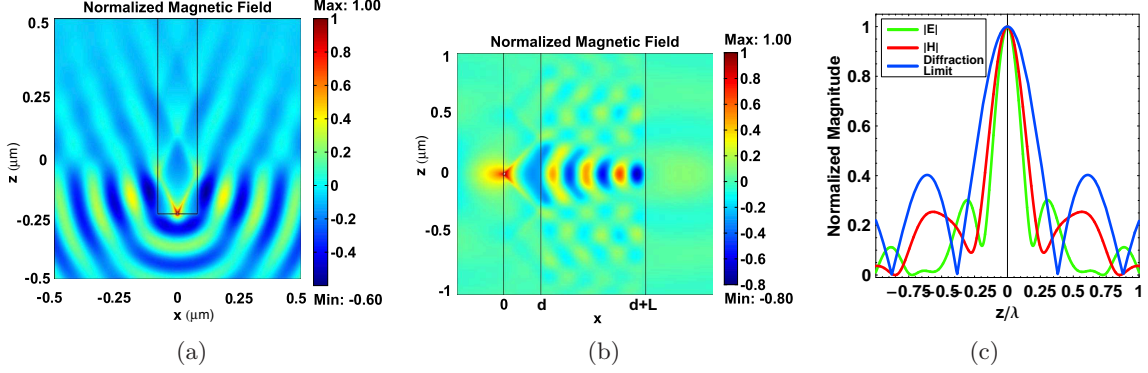
13

Figure 11: (a) H-field distribution of a Ag/SiO$_2$ bulk anisotropic leaky waveguide embedded in a Si host. The volume fraction for Ag is 0.2. The width of the slab is $0.16\,\mu$m. A magnetic current line source is located at $(x = 0, z = -0.25\,\mu$m$)$. $\lambda = 563.6\,$nm, $\epsilon_{\mathrm{Si}} = 16.3 + i0.26$, $\epsilon_{\mathrm{Ag}} = -11.89 + i0.83$, $\epsilon_{\mathrm{SiO_2}} = 2.13$, giving $\epsilon_x = -0.67 + i0.17$, $\epsilon_z = 2.79 + i9.05 \times 10^{-3}$. (b) A Ag/SiO$_2$ bulk anisotropic leaky waveguide juxtaposed with a Si slab, functioning as a sub-diffraction imaging system. The thickness of the waveguide $d = 0.16\,\mu$m, the thickness of silicon slab $L = 0.45\,\mu$m, and the surrounding medium is free space. The excitation current line source is located at $x = 0$. (c) The field profile at the image plane $x = d + L$.
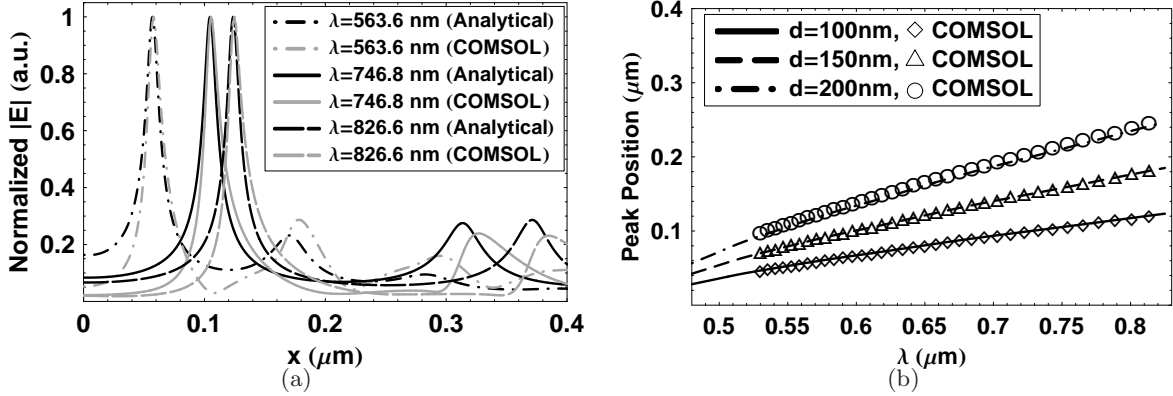

Figure 12: An anisotropic spectrometer. (a) Electric field magnitude at three wavelengths obtained from finite-element simulation and analytical results: a magnetic line current source radiates through an anisotropic Ag/ZnO slab with $D = 0.5$, and the slab thickness $d = 100\,$nm. (b) Variation of the position the principal peak as a function of wavelength for a homogenized Ag/ZnO stack slab.

We have investigated wave propagation behavior inside a cylindrically anisotropic metamaterial with a general parameter space $\epsilon_\phi \epsilon_\rho < 0$, and identified the shape of the resonance cones as two sets of logarithmic spiral curves [33]. The formation of resonance cones inside a curved film of cylindrically anisotropic material excited by a line source is applied to demonstrate a new spectrometer/multiplexer class that exploits metal-insulator stack metamaterials. A bilayer imaging system consisting of two cylindrically curved shells of such media, which holds promise for far-field sub-diffraction-limit imaging and obviates the strict condition of material parameters, has also been proposed [34].

14

8 Impact of Surface Roughness on the Effective Medium Parameters and Subwavelength Imaging

The effective dielectric constant for a multilayer metal-insulator stack is obtained from a numerical simulation and compared with the analytical result. The impact of the surface roughness for subwavelength imaging is established [35]. This work is now being prepared as a journal paper.

The evolution of nanofabrication techniques has allowed the fabrication of precise structures. However, the metal-insulator stacks that can yield far-subwavelength image resolution (see, for example, [1, 36]) require very smooth and very thin metal and insulator films. It is of importance to understand the influence of this inevitable roughness for the improved design of nanostructures and experiments. Here, we use a simple method for the effective medium parameter extraction for a metal-insulator planar slab and study the effect on the subwavelength imaging performance using silver (Ag) and zinc oxide (ZnO) as representative materials.

The numerical simulation used for the extraction procedure is carried out using an FEM solver (COMSOL Multiphysics [37]). The geometry consists of a 100 nm thick planar slab placed in vacuum and composed of alternate layers of Ag and ZnO. The two ports (left- and right-most boundaries) are located at a distance of 600 nm from each slab surface. The top and bottom boundaries are perfect electric conductors with a separation of 1 μm, forming a waveguide, and a TM wave is incident normally on the slab from the left side. The Ag and ZnO dielectric constants (ϵ_{Ag} and ϵ_{ZnO}, respectively) are obtained by interpolating measured bulk data [38,39]. The scattering parameters at the ports are obtained from the FEM simulation, and using these, the effective transverse dielectric constant is calculated according as [13]

$$\epsilon_{eff} = \frac{(1 - S_{11})^2 - S_{21}^2}{(1 + S_{11})^2 - S_{21}^2}, \qquad \mu_{eff} = 1. \tag{10}$$

We have assumed $\mu_{eff} = 1$ for our numerical simulations because the materials are non-magnetic. In the homogenization limit, the effective transverse dielectric constant for a planar slab with smooth surfaces depends on the duty cycle, D, and is analytically given by [40]

$$\epsilon_{eff} = \epsilon_{Ag}D + \epsilon_{ZnO}(1 - D). \tag{11}$$

Figure 13(a) shows ϵ_{eff} obtained numerically for a planar 100 nm thick Ag/ZnO multilayer slab for different numbers of periods, and compared with the analytical homogenized result in (11). It is observed that, in this case, 10 periods is sufficient to approach the homogenization limit. Figures 13(b) and (c) show the effect of the surface roughness on ϵ_{eff} for the 100 nm Ag/ZnO multilayer slab having 5 and 10 periods, respectively. As we increase the surface roughness, the deviation of ϵ_{eff} extracted from the numerical model increases, relative to that determined by the analytic result in (11). The standard deviation in ϵ_{eff} also increases with increase in surface roughness. It is thus clear that roughness has a substantial influence on the homogenized dielectric constant determined using the FEM model, which provides data that could be representative of a measurement.

To evaluate the impact of surface roughness in an imaging application, we perform another series of numerical studies. Figure 14(a) shows a stack having statistical roughness, and from a series of such calculations, we generated Fig. 14(b), which shows the impact on subwavelength resolution. These calculations assumed a standard deviation of around 1 nm, comparable with that achieved with e-beam evaporation and a 35 nm film thickness [41].

This work constitutes another step towards a better design of manufacturable stack-based nanostructures by improving our understanding of the impact of the surface roughness on the effective dielectric constant. The metal-insulator stack shows promise for subwavelength imaging and other applications.
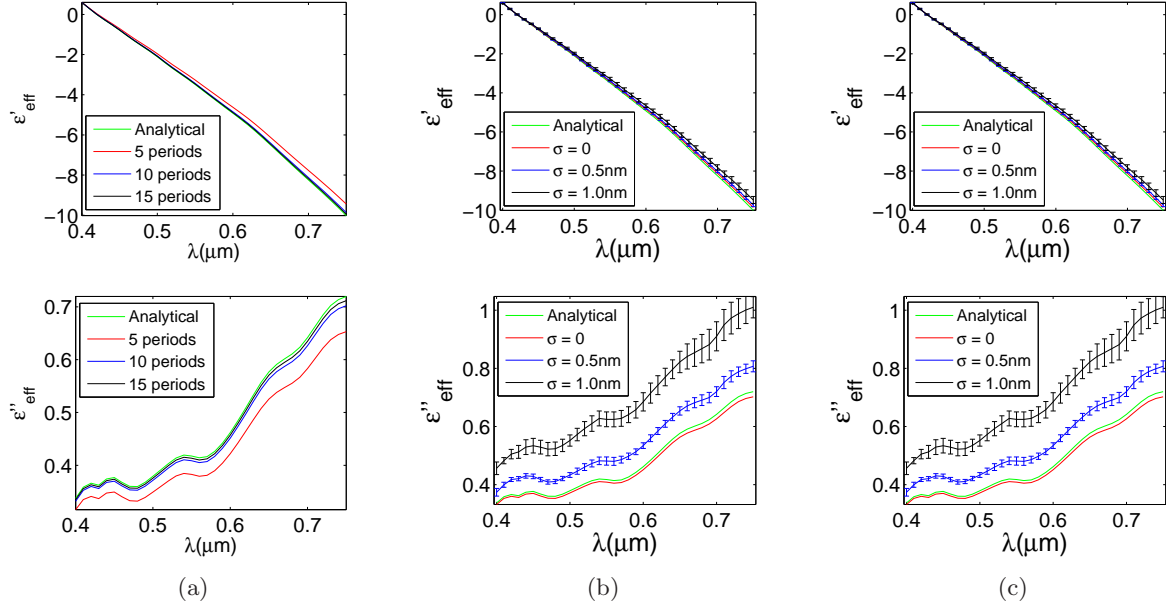
Figure 13: The real (top row) and imaginary (bottom row) part of the effective transverse dielectric constant, ϵ_{eff} obtained as a function of wavelength for the 100 nm Ag/ZnO multilayer slab. (a) ϵ_{eff} for different numbers of periods with smooth surfaces. (b) and (c) ϵ_{eff} for the slab with 5 and 10 periods, respectively, obtained for different standard deviations of the surface roughness, σ. The lines and the error bars show the mean and the standard deviation for the extracted ϵ_{eff}. The analytical result shown in green is obtained using (11), while the others are obtained from the FEM simulation and using (10).

9 Journal Papers Acknowledging this Award

Several forthcoming papers will acknowledge this award. Those published thus far that do so are as follows.

1. A. Ludwig and K. J. Webb. Dark materials based on graphene sheet stacks, *Opt. Lett.*. 36(2):106, Jan. 2011

2. K. J. Webb and Shivanand. Negative electromagnetic plane-wave force in gain media, *Phys. Rev. E.* 84:057602, Nov. 2011

3. H. Liu and K. J. Webb. Resonance cone formation in a curved cylindrically anisotropic meta-material film. *Opt. Lett.*, 36(3):343345, 2011

4. H. Liu and K. J. Webb. Resonance cones in cylindrically anisotropic metamaterials: a Green's function analysis. *Opt. Lett.*, 36(3):379381, 2011

5. Shivanand and K. J. Webb. Electromagnetic field energy density in homogeneous negative index materials. *Opt. Express*, 20(10):11370-11381, May 2012

6. K. J. Webb and Shivanand. Electromagnetic plane wave forces on homogeneous material. *J. Opt. Soc. Am. B*, 2012 (to appear)
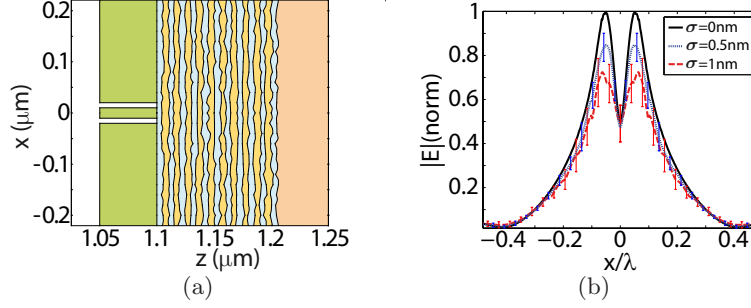
Figure 14: (a) The geometry considered for our numerical study of the influence of surface roughness in an anisotropic lens: a screen with two 10 nm slits and 30 nm center-to-center distance; Ag/ZnO multilayer stack with 5nm thick layers and a surface roughness with standard deviation σ; and incident field wavelength $\lambda = 413.3$ nm. (b) Statistical influence of random film roughness on the resolution in a double slit imaging arrangement, showing that achievable film smoothness should allow far subwavelength image resolution.

10   Conference Papers Describing the Results from this Research

1. H. Liu and K. J. Webb, An Anisotropic Metamaterial Leaky Waveguide. *2010 CLEO/QELS, Laser Science to Photonic Applications*, May 16-21, 2010, San Jose, California

2. H. Liu and K. J. Webb, Leaky-Wave Antennas with Anisotropic Metamaterials. *IEEE Antennas and Propagation Symposium*, July 11-17, 2010, Toronto, Canada

3. A. Ludwig and K. J. Webb, On the accuracy of effective medium parameter extraction procedures for optical metamaterial. *IEEE Antennas and Propagation Symposium*, July 11-17, 2010, Toronto, Canada

4. H. Liu and K. J. Webb, Resonance cones in cylindrically anisotropic metamaterials: a Green's function analysis. *OSA Frontiers in Optics,* Rochester, NY, Oct. 24-28, 2010

5. H. Liu and K. J. Webb, Optical devices based on cylindrically anisotropic metamaterials. *IEEE/OSA/APS CLEO/IQEC Meeting*, Baltimore, MD, May 1-6, 2011

6. Shivanand, A. Ludwig, and K. J. Webb, Impact of surface roughness on the effective dielectric constant and subwavelength image resolution of metal-insulator stack lenses. Digest of *OSA Frontiers in Optics*, San Jose, CA, Oct. 16-20, 2011

References

[1] H. Liu, Shivanand, and K. J. Webb. Subwavelength imaging opportunities with planar uniaxial anisotropic lenses. *Opt. Lett.*, 33(21):2568–2570, November 2008.

[2] W. Cai, U. K. Chettiar, A. V. Kildishev, and V. M. Shalaev. Optical cloaking with metamaterials. *Nature Photonics*, 1(1):224–227, April 2007.

[3] S. A. Cummer, B. I. Popa, D. Schurig, D. R. Smith, and J. B. Pendry. Full-wave simulations of electromagnetic cloaking structures. *Phys. Rev. E*, 74:036621, September 2006.

[4] K. J. Webb and A. Ludwig. Semiconductor quantum dot mixture as a lossless negative dielectric constant optical material. *Phys. Rev. B*, 78:153303(1–4), 2008.

[5] Shivanand, H. Liu, and K. J. Webb. Imaging performance of an isotropic negative dielectric constant slab. *Opt. Lett.*, 33(21):2562–2564, Nov 2008.

[6] K. J. Webb and J. Li. Resonant waveguide field enhancement in dimers. *Opt. Lett.*, 31(22):3348–3350, 2006.

[7] K. J. Webb and J. Li. Waveguide cavity surface-enhanced Raman scattering. *Phys. Rev. B*, 73(7):73404, 2006.

[8] C. A. Leatherdale, W. K. Woo, F. V. Mikulec, and M. G. Bawendi. On the absorption cross section of CdSe nanocrystal quantum dots. *J. Phys. Chem. B*, 106(31):7619–7622, 2002.

[9] A. B. Kuzmenko, E. van Heumen, F. Carbone, and D. van der Marel. Universal optical conductance of graphite. *Phys. Rev. Lett.*, 100(11):117401, 2008.

[10] T. Stauber, N. M. R. Peres, and A. K. Geim. Optical conductivity of graphene in the visible region of the spectrum. *Phys. Rev. B*, 78(8):085432, 2008.

[11] K. F. Mak, M. Y. Sfeir, Y. Wu, C. H. Lui, J. A. Misewich, and T. F. Heinz. Measurement of the optical conductivity of graphene. *Phys. Rev. Lett.*, 101(19):196405, 2008.

[12] A. Ludwig and Webb K. J. Dark materials based on graphene sheet stacks. *Opt. Lett.*, 36(2):106, Jan. 2011.

[13] A. Ludwig and K. J. Webb. Accuracy of effective medium parameter extraction procedures for optical metamaterials. *Phys. Rev. B*, 81(11):113103, Mar 2010.

[14] L. Ci, L. Song, D. Jariwala, A. L. Elías, W. Gao, M. Terrones, and P. M. Ajayan. Graphene shape control by multistage cutting and transfer. *Advanced Materials*, 21(44):4487–4491, 2009.

[15] Z. P. Yang, L. Ci, J. A. Bur, S. Y. Lin, and P. M. Ajayan. Experimental observation of an extremely dark material made by a low-density nanotube array. *Nano Letters*, 8:446–451, 2008.

[16] D. R. Smith, S. Schultz, P. Markoš, and C. M. Soukoulis. Determination of effective permittivity and permeability of metamaterials from reflection and transmission coefficients. *Phys. Rev. B*, 65:195104, 2002.

[17] R. Loudon. The propagation of electromagnetic energy through an absorbing dielectric. *J. Phys. A*, 3:233–245, 1970.

[18] R. Ruppin. Elecromagnetic energy density in a dispersive and absorptive material. *Phys. Lett. A*, 299:309–312, 2002.

[19] S. A. Tretyakov. Electromagnetic field energy density in artificial microwave materials with strong dispersion and loss. *Phys. Lett. A*, 343:231–237, 2005.

[20] A. D. Boardman and K. Marinov. Electromagnetic energy in a dispersive metamaterial. *Phys. Rev. B*, 73:165110, 2006.

[21] T. J. Cui and J. A. Kong. Time-domain electromagnetic energy in a frequency-dispersive left-handed medium. *Phys. Rev. B*, 70:205106, 2004.

[22] F. D. Nunes, T. C. Vasconcelos, M. Bezerra, and J. Weiner. Electromagnetic energy density in dispersive and dissipative media. *J. Opt. Soc. Am. B*, 28(6):1544–1552, Jun 2011.

[23] R. W. Ziolkowski. Superluminal transmission of information through an electromagnetic medium. *Phys. Rev. E*, 63:046604, 2001.

[24] K. J. Webb and Shivanand. Electromagnetic field energy in dispersive materials. *J. Opt. Soc. Am. B*, 27(6):1215–1220, Jun 2010.

[25] Shivanand and K. J. Webb. Electromagnetic field energy density in homogeneous negative index materials. *Opt. Express*, 20(10):11370–11381, May 2012.

[26] K. J. Webb and Shivanand. Negative electromagnetic plane-wave force in gain media. *Phys. Rev. E*, 84:057602, Nov 2011.

[27] K. J. Webb and Shivanand. Electromagnetic plane wave forces on homogeneous material. *J. Opt. Soc. Am. B*, 2012. to appear.

[28] E. F. Nichols and G. F. Hull. The pressure due to radiation. *Phys. Rev. (Series I)*, 17:26–50, 1903.

[29] A. Einstein. On the quantum theory of radiation. *Phys. Z.*, 18:121, 1917.

[30] H. Liu and K. J. Webb. Leaky wave radiation from planar anisotropic metamaterial slabs. *Phys. Rev. B*, 81(20):201404, 2010.

[31] H. Liu and K. J. Webb. Subwavelength imaging with nonmagnetic anisotropic bilayers. *Opt. Lett.*, 34(14):2243–2245, 2009.

[32] H. Liu and K. J. Webb. Approximate Green's function for a uniaxially anisotropic metamaterial slab, and its application in analyzing a spectrometer. *Opt. Lett.*, 35(11):1869–1871, 2010.

[33] H. Liu and K. J. Webb. Resonance cone formation in a curved cylindrically anisotropic metamaterial film. *Opt. Lett.*, 36(3):343–345, 2011.

[34] H. Liu and K. J. Webb. Resonance cones in cylindrically anisotropic metamaterials: a Green's function analysis. *Opt. Lett.*, 36(3):379–381, 2011.

[35] Shivanand, A. Ludwig, and K. J. Webb. Impact of surface roughness on the effective dielectric constant and subwavelength image resolution of metal-insulator stack lenses. In *Frontiers in Optics*, page JTuA11. OSA, 2011.

[36] H. Liu, Shivanand, and K. J. Webb. Subwavelength imaging with nonmagnetic anisotropic bilayers. *Opt. Lett.*, 34(14):2243–2245, July 2009.

[37] COMSOL Multiphysics. http://www.comsol.com/products/multiphysics/.

[38] E. D. Palik. *Handbook of Optical Constants of Solids*. Academic Press, 1998.

[39] W. L. Bond. Measurement of the refractive indices of several crystals. *J. Appl. Phys.*, 36(5):1674–1677, 1965.

[40] K. J. Webb and M. Yang. Subwavelength imaging with a multilayer silver film structure. *Opt. Lett.*, 31(14):2130–2132, Jul 2006.

[41] N. Fang, H. Lee, C. Sun, and X. Zhang. Sub-diffraction-limited optical imaging with a silver superlens. *Science*, 308:534–537, Apr. 2005.